Research Square

Preprints are preliminary reports that have not undergone peer review.
They should not be considered conclusive, used to inform clinical practice,
or referenced by the media as validated information.

# Direct-Write Transfer Printing of Low-Loss Copper Interconnects onto Arbitrary Substrates

**Yuxin Jiao**
The University of Texas at Dallas
**Andrew Gleadall**
Loughborough University
**Timothy D. Hall**
Faraday Technology Inc
**Majid Minary-Jolandan**
majid.minary@utdallas.edu

The University of Texas at Dallas

**Article**

**Keywords:** Meniscus-confined electrodeposition, transfer printing, additive manufacturing, copper interconnects, conductor loss, flexible electronics, smart textiles

**Posted Date:** August 14th, 2026

**DOI:** https://doi.org/10.21203/rs.3.rs-10491101/v1

**License:** This work is licensed under a Creative Commons Attribution 4.0 International License.
Read Full License

**Additional Declarations:** No competing interests reported.

# Abstract

Conformal and wearable electronic systems, from smart textiles to bioelectronics, increasingly require metal interconnects capable of operating at gigahertz-to-millimeter-wave frequencies for wireless communication and power transfer. At these frequencies, the skin effect confines current to a nanometer-scale surface layer, so conductor loss is governed jointly by the resistivity and the surface roughness of the metal, both of which are set by the deposition process. However, existing metallization routes each sacrifice one of these properties: vapor-phase deposition yields smooth, near-bulk copper but requires vacuum, elevated temperature, and line-of-sight access that excludes porous and textured substrates, while particle-based inks pattern freely on arbitrary substrates but leave porous, rough films that recover one property only at the expense of the other. Here, we demonstrate a direct-write transfer printing process that decouples copper deposition from the target substrate: copper is written by meniscus-confined electrodeposition onto a stainless-steel cathode and then transferred intact onto the receiver substrate, without masks, vacuum, or a thermal budget. Deterministic control over nozzle position, velocity, and dwell time allows closed-path and geometrically complex patterns to be written without the seam defects and delamination that arise from slicer-generated paths designed for conventional extrusion. Copper patterns were transferred onto substrates spanning polymer films, adhesive tapes, and woven and nonwoven textiles, preserving feature geometry and linewidths down to 550 μm. The transferred films presented a smooth, substrate-templated working surface with 40–55 nm roughness and near-bulk resistivity of 2.3–2.6 μΩ·cm, yielding surface resistance within 1.2 times that of bulk copper and conductor loss 1.4 to 7.1 times lower than printed copper across 5–30 GHz, while withstanding handling and mounting as free-standing foils. By separating metal growth from the receiving surface, this approach provides a mask-free, vacuum-free route to gigahertz-compatible copper interconnects on arbitrary and textured substrates, opening a pathway toward high-frequency smart textiles and conformal bioelectronics.


# Introduction

Conformal and wearable electronic systems are progressing beyond quasi-static sensing toward frequency-dependent operation, in which wireless communication and power transfer at gigahertz to millimeter-wave frequencies are integral to device function [1–3]. At these frequencies the deposited metal itself becomes a performance-limiting component, and that demand extends to nonplanar and compliant substrates where the metallization must conform to the surface it serves [2,4]. Signal attenuation in these interconnects arises from two sources: dielectric loss, set by the substrate, and conductor loss, set by the metal. Dielectric loss is fixed once the substrate is chosen; conductor loss, by contrast, is inherited from the process that deposits the metal. Conductor loss originates in the finite resistivity of the metal and is governed by how current distributes through the conductor at high frequency. As frequency increases, the skin effect confines current toward the surface, narrowing the conducting layer to a skin depth of roughly 380–470 nm in copper across the 20–30 GHz band [5,6]. When the film is thicker than this skin depth, surface resistance sets conductor loss: it rises with resistivity

above the bulk copper value of 1.72 μΩ·cm, arising from microstructural defects, and with roughness of the current-carrying surface on the scale of the skin depth.

Deposition establishes both properties: the method governs the microstructure that determines resistivity, while the growth surface transmits its topography to the current-carrying face. These two levers frame the typical routes to metallizing compliant substrates, vapor-phase deposition and particle-based inks, each of which compromises at least one property, particularly on textured surfaces.

Vapor-phase deposition remains the benchmark for smooth, low-resistivity metal films, and recent advances have extended it toward soft and freeform electronics. It has been reported that seed-layer-assisted sputtering can direct silver onto a 1 nm copper nucleation layer, forming continuous films with surface roughness below 0.5 nm at thicknesses of a few nanometers[7]. Stress-regulated dry transfer printing has been shown to lift sputtered copper films from rigid donor wafers and rebond them to polyethylene terephthalate, and the transferred electrodes demonstrated 500 bending cycles at a 10 mm radius[8]. Area-selective evaporation can replace the rigid shadow mask with printed metal-vapor-desorption layers that repel incoming vapor, patterning films directly on stretchable, non-developable surfaces [9]. Line-of-sight vapor flux, however, remains intrinsic to evaporation regardless of masking strategy, so porous and fibrous substrates such as textiles and nonwovens still present shadowed faces the vapor cannot reach [9]. Near-bulk resistivity is likewise demanding of process conditions: reaching 2.85 μΩ·cm requires a base pressure below $6.4 \times 10^{-4}$ Pa, a substrate temperature of 300°C that most polymers do not survive, and several hours of sputtering [8]. Transferring that film onto a flexible receiver substrate raises the resistivity to 3.1 μΩ·cm, reflecting microcracking introduced during peel-off [8].

Particle-based inks deposit under ambient conditions and pattern digitally on substrates that vacuum and line-of-sight exclude, from polymer films to fabrics [10]. Hydrogen plasma sintering has been shown to fully densify inkjet-printed copper tracks on polyethylene terephthalate at low temperature, and the densified tracks reached 3.23 μΩ·cm, 1.82 times the bulk value [11]. Direct screen-printing has been utilized to lay silver coplanar waveguides onto nonwoven textiles without any surface modification of the fabric, transmitting signals from 0.5 to 10 GHz [12]. Ultraviolet-curable inks can eliminate thermal sintering altogether: cured on nylon fabrics, they form circuits with conductivities of $6.02 \times 10^{6}$ S $m^{-1}$ and antennas that read beyond 3 m after five wash cycles [13]. Printed films, however, concede one of the two properties that govern surface resistance, and rarely both together. Residual porosity and particle boundaries hold resistivity above the bulk value; even full densification leaves it nearly twice as high [11]. Recovering smoothness costs the resistivity back: a sequence of photosintering, silver infiltration, and cold rolling has been reported to reach a roughness of 0.28 μm, below the skin depth across the 20–30 GHz band, but resistivity climbed to 8.32 μΩ·cm, nearly five times bulk [14]. On fabric the penalty compounds rather than trades off. The wet ink conforms to the fibers beneath it, so the printed conductor inherits the textile's surface roughness of 18 μm, roughly forty times the skin depth above 20 GHz [12].

Electrodeposition offers a different balance. It produces dense copper at near-bulk resistivity without vacuum or a thermal budget, but conventional plating deposits across the entire conductive cathode and provides no control over where copper forms. Meniscus-confined electrodeposition (MCED) localizes the redox reaction to an electrolyte meniscus beneath a nozzle, which enables direct writing of copper into arbitrary planar geometries [15–17]. The primary constraint is that the reaction requires a conductive surface. Producing conductors on dielectric substrates therefore relies on a blanket seed coating, followed by direct writing and a subsequent etch to clear the seed. This reinstates the subtractive steps that direct writing is meant to remove. It also excludes the substrates where additive metallization is needed most. Smart textiles build sensing and actuation directly into the fabric, and their design and manufacture cannot accommodate blanket seed layers or immersion in etchants [18–21].

Here, we introduce a substrate-independent route that separates deposition from the final substrate: copper is deterministically deposited by MCED on a stainless-steel conductor and then transferred onto the target substrate (Fig. 1). A user-defined G-code toolpath drives the nozzle across the substrate, with deterministic control over position, velocity, and dwell time, writing copper into arbitrary planar geometries - including closed paths - by confining the electrolyte meniscus to the wetted footprint beneath the nozzle tip (Fig. 1A, B). Following deposition, a transfer tape is brought into contact with the copper film, pressure is applied uniformly, and peeling exploits the differential adhesion between the copper-tape and copper-steel interfaces to lift the film cleanly onto the receiver substrate (Fig. 1C). The process requires no masks, resists, vacuum, or thermal budget. The resulting films exhibit a smooth, substrate-templated working surface with near-bulk resistivity, yielding conductor loss substantially below that of printed copper across the 5–30 GHz band, while withstanding handling and mounting as free-standing foils. (See Movies S1 and S2).

## Results

To demonstrate substrate and geometry versatility, copper patterns were transferred onto a range of receiver substrates (Fig. 2). A serpentine trace with spiral-filled bonding pads was transferred onto a cast PVDF-TrFE film (Fig. 2A), and a spiral coil and a closed circular loop were transferred onto Kapton tape (Fig. 2B, C). Together these geometries span open paths (single trace lines), filled areas (bonding pads), and closed paths (intersecting edges), all of which transferred intact. Transfer was further demonstrated onto substrates of diverse material and surface texture: a coarse woven fabric, a nonwoven electrospun mat, and an electroplating tape carrying a closed rectangular loop (Fig. S1). Beyond substrate diversity, feature resolution was preserved: linewidths from 1.5 mm down to 550 μm transferred intact (Fig. S2).

Two behaviors of localized electrodeposition must be accounted for when designing for closed-path geometries: preferential deposition, which governs where copper grows, and film stress, which governs whether the grown film survives [22–25]. Deposition favors existing copper over bare steel: the overpotential for growth on a native surface is lower than for heterogeneous nucleation [26,27]. The growing deposit also depletes $Cu^{2+}$ locally, and its diffusion field intercepts incoming ions before they reach the adjacent seam. The seam is mass-transport starved and does not close on its own. Raising the

current density fills starved seams but drives deposition further from equilibrium, trapping defects that accumulate as intrinsic film stress. Stored stress relaxes through intra-film fracture and interfacial delamination (Figs. S3 and S4). Left unaddressed, this starvation and stress buildup causes the film to delaminate prematurely or unevenly during peel, so the toolpath must be designed to prevent it during growth rather than compensate for it afterward.

The FullControl-based toolpath addresses this directly by enabling deterministic control over the position, velocity, and time of every nozzle move in sequence[28]. Rather than generating motion through a fixed slicing algorithm, FullControl represents manufacture as an explicitly ordered sequence of kinematic and process-state changes. It can generate any command supported by the machine controller's CNC command language, including position, feed rate, dwell, tool or process-state changes, and other controller-specific instructions. In this work, it was used to directly define the nozzle trajectory, speed, dwell locations and repeated deposition passes parametrically. This makes it possible to design the path around the electrochemistry itself, rather than around assumptions built for volumetric extrusion. For example, in Fig. 2A the square-line connection required a spiral fill pattern for both pads; however, the second pad required a dwell over its center. When printing a closed hollow shape such as a circle (Fig. 2C), a repeated back-and-forth arc is inserted to fill the connection point.

Commercial slicers generate paths under volumetric extrusion assumptions, in which deposited material scales with nozzle travel and every location on the part is equivalent. Neither holds for electrodeposition, where growth depends on the underlying surface and the local exposure time. The resulting workflow enables arbitrary planar geometries, including filleted corners, overlapping spiral fills, and closed paths, to be written and transferred in a single process. Together, Figs. 2 and S1 demonstrate transfer onto substrates spanning flexible films and woven and nonwoven textiles, illustrating the breadth of substrate morphologies the process can access; extension to additional substrate classes should be achievable with minor process optimization.

A prerequisite for reliable transfer printing is that the deposited film has sufficient mechanical integrity to withstand delamination and handling as a free-standing foil (Fig. 3). To establish this, copper traces were written onto stainless steel using MCED, in which growth is confined to the wetted footprint beneath a translating nozzle. A 20 mm line was built over 20 successive passes at 2 mm $s^{-1}$, with a 5 mm sacrificial runway at each end to stabilize the meniscus before it reached the active trace region. Time-lapse imaging at 4 s, 64 s, and 124 s captures the progressive build-up from a single-pass seed layer to a continuous, mechanically coherent film (Fig. 3A). At 124 s, spontaneous delamination is visible at the terminal end of the trace, where extended electrolyte exposure locally thickens the film and initiates edge lifting. This is consistent with delamination initiating preferentially at film edges, characterized in detail in Fig. S3.

Maintaining a constant nozzle velocity across the entire trace produces a uniform thickness profile with no periodic thickness features, in contrast to the start-stop profile, where programmed pauses locally thicken the film and trigger premature delamination at those sites (Fig. S5). The motion system's

acceleration limits were not expected to have a considerable effect on this profile. Clean release depends on both this uniformity and sufficient overall thickness: films below ~ 1 μm fractured on peeling regardless of profile, while films of ~ 2 μm and above delaminated intact, as shown across a wider thickness range in Fig. S6. The delaminated film is readily handled as a free-standing foil without fracture (Fig. 3B), confirming sufficient mechanical integrity for transfer.

To quantify the mechanical response of the transferred films, tensile testing was performed on free-standing copper strips across a thickness range of 1–4 μm ($n$ = 3) (Fig. 3C, D). Films were transferred by water-assisted lift-off, in which surface tension separates Cu from steel without applied peel force. The films sustained stresses up to approximately 224 ± 77.3 MPa before fracturing at strains below 0.52 ± 0.25%. This variability reflects the expected sensitivity of thin-film mechanical properties to thickness and grain structure, and strength and ductility fall below bulk copper accordingly [29–32]. For the transfer process itself, the measured strength is sufficient: delaminated MCED films across the 1–4 μm range survive lift-off, manipulation, and mounting as free-standing foils, confirming they are mechanically robust enough for the free-standing transfer central to this work.

Having established that delaminated films are mechanically viable for transfer, we next characterize the surface morphology and thickness control of the copper films. These two properties directly govern high-frequency electrical performance. Delamination produces copper films with two morphologically distinct faces, and understanding which face carries current after transfer is central to predicting conductor loss. Surface roughness was mapped by laser confocal microscopy at a 3×5 grid of positions spanning the width and length of the 20 mm trace (Fig. 4A, inset) and is reported as the areal root-mean-square roughness ($S_q$). The substrate-facing surface, cast against the polished stainless steel during deposition and exposed only after transfer, is smooth and spatially uniform ($S_q$ 40–55 nm) across the full 20 mm deposit. The free growth front (nozzle side) exposed to the electrolyte is rougher and more variable ($S_q$ 200–660 nm), with a modest increase toward the trace's end due to extended electrolyte exposure as deposition concludes (Fig. 4A). SEM confirms the same contrast at the microstructural level: the substrate side is smooth and featureless, reproducing the finish of the polished steel it grew against, while the nozzle side is granular and nodular (Fig. 4B).

Laser confocal height maps of the bare stainless steel and both copper faces make this inheritance explicit. The substrate side mirrors the smooth, striated character of the polished steel, while the nozzle side presents a rougher, island-like topography (Fig. S7). This asymmetry constitutes a structurally advantageous feature of the transfer-printing architecture. The receiver substrate preferentially contacts the nozzle side, thereby presenting the smoother copper-steel interface as the functional surface. The nozzle-side roughness reflects the underlying grain morphology of the growth front. Plan-view SEM of the nozzle-facing surface at two film thicknesses reveals a clear contrast: the ~ 1.2 μm film shows a dense, uniform population of fine equiaxed grains, while the ~ 3.5 μm film exhibits coarser, nodular grains with a more irregular feature (Fig. S8).

This transition from fine equiaxed to coarser nodular morphology with increasing thickness is consistent with a progression from nucleation-dominated growth at early stages to growth increasingly controlled by coalescence and mass transport as the film thickens. Thickness is controlled directly by the number of deposition passes, a relationship governed by Faraday's law, where plated thickness scales with the total charge passed:

$$t = \frac{MQ}{nF\rho_m A} \quad \text{Eq. 1}$$

(*M* molar mass, *Q* charge, *n* = 2, *F* Faraday's constant, *ρ*□ copper density, *A* deposit area). Because each pass delivers a nominally fixed charge over the same footprint, thickness accumulates in direct proportion to pass count. The film grows at a constant rate of ~ 0.13 µm per layer, building linearly from ~ 0.75 µm at 5 layers to ~ 4.1 µm at 30 layers (Fig. 4C), making layer count a straightforward and predictable route to a target thickness without requiring real-time feedback or process adjustment. The minimum viable thickness for clean transfer (established in Fig. 3 and Fig. S6) falls near ~ 2 µm, and the linear growth rate means this threshold is reliably reached within approximately 15 layers under the deposition conditions used here.

Having established the surface morphology and thickness control of the transferred films, we next evaluate their electrical quality in Fig. 5. Specifically, we assess whether resistivity and surface roughness are simultaneously compatible with low-loss high-frequency transmission. Conductor loss scales directly with surface resistance ($\alpha \propto R_s$). Surface resistance is in turn governed by two material properties: resistivity and roughness. The skin depth is $\delta = \sqrt{(\rho/\pi f \mu_0)}$, where $\rho$ is the resistivity, $f$ the frequency, and $\mu_0 = 4\pi \times 10^{-7}$ H·m$^{-1}$. At low frequency, current occupies the full film cross-section. Sheet resistance $R_{\square} = \rho/t$ therefore decreases with increasing film thickness. Once film thickness exceeds the skin depth, the skin effect confines current to a surface layer one skin depth thick, and sheet resistance gives way to surface resistance $R_s = \rho/\delta$. In this regime, surface resistance depends on resistivity alone. Additional thickness yields no further reduction in conductor loss. Roughness comparable to the skin depth lengthens the effective conduction path and raises the surface resistance. Simultaneous minimization of resistivity and surface roughness, therefore, constitutes the central material requirement for a high-frequency conductor. Figure 5 evaluates the transferred films against this requirement.

Figure 5A presents an Ashby plot of surface roughness against resistivity, positioning confined electrodeposition against ink-based deposition of copper. The skin depth at 5, 20, and 30 GHz is marked by horizontal reference lines, and bulk copper resistivity by a vertical reference. Printed conductors scatter across the upper right of the plot, where residual porosity and organic content elevate resistivity and particle-based film formation produces roughness that meets or exceeds the skin depth above 20 GHz. Confined electrodeposition occupies the lower-left corner, the only region of property space in which near-bulk resistivity coincides with roughness below the skin depth across the full 5 to 30 GHz band. This position is not an absolute bound, as ink-based routes can surpass the transferred films in a single property. Near-bulk resistivity and nanometer-scale smoothness have been reported[11,33,34]. Both achievements, however, rely on multi-step post-processing, such as galvanic displacement with

electroplating, vacuum hydrogen plasma sintering, or sequential drying with near-infrared and intense pulsed light treatments.

The improvement is moreover restricted to a single axis, and the gain in one property is conceded in the other. Confined electrodeposition attains this region of property space in a single deposition step followed by transfer. Table S1 quantifies the comparison through the effective surface resistance at 20 GHz with a Hammerstad roughness correction [35]. On this basis, the substrate face of confined-electrodeposited copper delivers 1.4 to 2.4 times lower surface resistance than moderate-roughness inkjet- and screen-printed copper. The advantage rises to 4.1 times against the most resistive inkjet films and 4.2 to 7.1 times against the roughest printed conductors[5,6,35].

Four-point-probe measurements confirm that this resistivity advantage is robust across the transfer-relevant thickness range (Fig. 5B). The thinnest transferred film (1.31 μm) measures ~ 3.5 μΩ·cm with a standard deviation of ± 0.72 μΩ·cm. The elevated scatter is attributed to fracture during transfer, confirmed in Fig. S6. Across the 2–4 μm regime, resistivity clusters at ~ 2.3–2.6 μΩ·cm (~ 1.3–1.5× bulk) and is statistically flat (one-way ANOVA, $P = 0.71$, $\eta^2 = 0.15$), with scatter dropping to ± 0.06–0.12 μΩ·cm, confirming that films of ~ 2 μm and above deliver low, reproducible resistivity print-to-print. At ~ 2.5 μΩ·cm, the resulting surface resistance is ~ 22, ~44, and ~ 54 $m\Omega.sq^{-1}$ at 5, 20, and 30 GHz, within 1.2× of bulk copper across the band. Delaminated confined-electrodeposited copper therefore combines the geometric freedom of a printed process with electrical performance approaching that of dense electrodeposited foil, making it well suited to low-loss radiofrequency and millimeter-wave interconnects on flexible and textile substrates.

## Discussion

This work establishes direct-write transfer printing as a route to gigahertz-compatible copper interconnects on substrates that existing metallization methods cannot serve. By separating copper growth - via meniscus-confined electrodeposition on a reusable stainless-steel cathode - from the substrate that ultimately carries it, the process removes the vacuum, thermal budget, and line-of-sight constraints that limit vapor-phase deposition. It also avoids the porosity and post-processing burden of particle-based printing. Deterministic toolpath control extends this approach to arbitrary planar geometries, including closed paths and filled pads, at linewidths down to 550 μm, and transfer was demonstrated across polymer films, adhesive tapes, and woven and nonwoven textiles. The resulting films present a smooth, substrate-templated working surface (40–55 nm roughness) with near-bulk resistivity (2.3–2.6 μΩ·cm), delivering surface resistance within 1.2× of bulk copper and conductor loss 1.4 to 7.1 times lower than printed copper across 5–30 GHz, while remaining mechanically robust enough for free-standing handling and transfer.

These results reframe metallization as a two-step problem - deposition and placement decoupled from one another - rather than a single process that must simultaneously pattern, densify, and conform to the target surface. This decoupling is particularly consequential for substrate classes, such as woven and

nonwoven textiles, that are incompatible with vacuum processing and difficult for inks to wet uniformly. It suggests that other receiver materials unable to withstand deposition-stage temperatures or chemistries could access comparable metal quality through the same route. Realizing this potential will require extending toolpath control to multilayer and higher-throughput geometries and validating transferred interconnects within functional radiofrequency devices. Although motion was the only toolpath variable controlled in this study, the same explicit, sequence-based toolpath representation could extend to synchronous control of motion and process parameters together - for example, varying local current density between corners and straight segments, or adjusting deposition parameters in real time from in-line inspection data during printing. Realizing these capabilities is the natural next step toward establishing transfer-printed electrodeposition as a general-purpose metallization strategy for high-frequency flexible, wearable, and textile electronics.

# Methods

**Printer Setup**: The print head assembly comprised three main components: a 16-gauge luer lock nozzle (outer diameter 1.65 mm, inner diameter 1.2 mm), a Y-connector with two female luer locks and one male luer spin lock, and an anode/electrolyte feed system. The nozzle was affixed to the male port of the Y-connector. A 5 mL syringe housing an epoxied copper wire anode was inserted into the straight section of the Y-connector, and the branch port was coupled via PTFE tubing to a 10 mL syringe, mounted on a syringe pump (NE-300, New Era Pump Systems) and pre-filled with commercial copper electrolyte (Transene Company). The anode syringe was mounted on an XYZ motorized linear stage (150 mm displacement range, Newport Corporation), and motion was programmed in G-code and translated into Tool Control Language (TCL) for execution by the Newport controller, enabling precise patterning in the XY plane. Deposition current was regulated using a VersaSTAT-4 Potentiostat/Galvanostat (Princeton Applied Research) in pulsed galvanostatic mode with a 50% duty cycle (On Time = 0.001 s, Off Time = 0.001 s). Current pulsing and nozzle motion operated independently, without explicit synchronization: because the 2 ms pulse period is orders of magnitude shorter than the time the nozzle spends at any position along the path, local deposition tracked residence time directly, and no handshake between the potentiostat and motion controller was required. Polished stainless steel sheet served as both the cathode and the print bed.

**Print-Path design**: Print paths were designed in Python using the open-source FullControl library, which represents a toolpath as an ordered list of coordinate points and motion-speed objects, allowing geometry, feed rate, and dwell placement to be defined parametrically in code. A custom post-processor converted each design into G-code for the deposition stage, writing all motion in relative positioning mode (G91) with each move issued as a linear command (G1) specifying X and Y displacement and feed rate. Every path began with a single approach move from the fixtured origin to the path start, followed by repeated traversals of the same trace at a constant feed rate of 2 mm $s^{-1}$. The start-stop comparison (Fig. S5) instead used a seed layer at 1.5 mm $s^{-1}$ followed by repeat layers at 15 mm $s^{-1}$, with four programmed 0.5 s pauses per layer. Four toolpath geometries were used: a straight multi-layer line, a

circular loop approximated as a closed polyline, a spiral of filleted concentric rectangular tracks, and a start-stop line with programmed dwell points.

**Applied current density**

The applied current density was determined for each sample from the measured deposit thickness via Faraday's law for the $Cu^{2+} + 2e^- \rightarrow Cu$ reaction

$j = \varphi(nF\rho\delta) / (Mt\eta)$ where $\rho$ = 8.96 g $cm^{-3}$, $M$ = 63.55 g $mol^{-1}$, $n$ = 2, F = 96,485 C $mol^{-1}$, $\varphi$ = 0.5 (duty cycle), $\eta$ = 1 (assumed current efficiency), and $t$ the total deposition time. Thickness was measured by stylus profilometry across six samples spanning 5–30 printed layers on 1.5 × 20 mm line segments, giving a mean current density of 19.4 ± 1.5 mA $cm^{-2}$.

**Substrate Transfer**: Following pattern deposition, the electrolyte was removed by blotting with a cleanroom wipe, followed by two to three deionized water rinses applied via pipette, and finally dry with a cleanroom wipe. Transfer was performed by press-stamping: a flexible substrate coated with pressure-sensitive adhesive was brought into contact with the printed copper. Pressure was applied across the film by hand, followed by additional pressure to ensure uniform contact. The substrate was allowed to dwell approximately 30 seconds before peeling, therefore lifting the copper film from the stainless-steel print bed. For the PVDF-TrFE substrate, the polymer solution was instead cast directly over the printed copper, dried overnight at room temperature, and peeled from the print bed, lifting the copper film with the cast film.

**Four-point probe**: Electrical resistivity was measured using an Ossila four-point probe with soft spring-loaded tips (1–1.4 mm displacement range, integrated micrometer for thickness input). Copper films were delaminated onto polyimide tape and prepared as 1.5 mm × 20 mm strips. Three measurements were taken per sample: one at the midpoint and one each offset to the left and right of center along the length. Resistivity was calculated assuming rectangular geometry with appropriate thickness corrections, averaged over 50 measurement points per probe contact.

**Thickness and surface roughness measurements**

Film thickness was measured with an Alpha-Step stylus profiler (KLA) using a diamond stylus tip at a contact force of 5–10 mg, scan rate of 50 μm $s^{-1}$, 100 μm vertical range, and 32-point averaging over a single forward scan. Baseline correction was applied in the KLA software by referencing the substrate level at the rising and falling edges of the copper film to remove the broad background introduced by substrate curvature. Three scans were taken per film and averaged to give a representative thickness profile.

Surface roughness was measured by 3D laser scanning confocal microscopy (VK-X3000, Keyence) in confocal mode using a 50× objective (Z pitch 0.5 μm, optical zoom 1.0×, laser intensity auto-adjusted at focus). Both faces of the delaminated film were characterized independently: the nozzle-facing surface was measured on the as-deposited film, and the substrate-facing surface was measured after transfer.

Substrate form was removed in Gwyddion by plane leveling followed by fourth-order polynomial flattening.

**Scanning Electron Microscopy (SEM)**

Free-standing copper films were obtained by water-assisted lift-off from the stainless-steel substrate. To image both faces, one end of a film was fixed to an aluminum SEM stub with double-sided copper tape and the film fractured by pulling, yielding two halves. One half was mounted substrate-face up and the other nozzle-face up, with the free end of each half secured with double-sided copper tape to keep both faces taut and flat. Films were imaged without a conductive coating, exploiting the intrinsic conductivity of copper. Imaging was performed on a Zeiss SIGMA 500 VP field-emission SEM at 8.00 kV accelerating voltage, ~ 13 mm working distance, using the SE2 secondary electron detector in high-vacuum mode with a 30 μm aperture.

**Tensile testing.** Free-standing copper films (20 mm length, 1.3 to 1.5 mm width) were mounted onto laser-cut C-frames for handling and alignment. The film ends were bonded to the frame tabs with two-part epoxy, and the 12 mm gap between the mounting tabs defined the gauge length. Tests were performed on a DMA ElectroForce 3200 Series III (TA Instruments) under displacement control at 50 μm $min^{-1}$, using a 225 N load cell and stock tensile grips. The frame tabs were clamped in the grips without contacting the epoxy. Before each test, the C-frame was cut twice along its length, leaving a small gap on each side, so that the load path passed only through the film. Engineering stress and strain were calculated with a custom MATLAB script from the measured force and displacement, using the film thickness and width measured with an Alpha-Step stylus profiler (KLA).

# Declarations

Author Contributions

Yuxin Jiao (methodology, investigation, data curation, writing, visualization), Andrew Gleadall (methodology), Timothy D. Hall (methodology), Majid Minary-Jolandan (conceptualization, methodology, writing)

**Acknowledgement**

This work is supported by the US National Science foundation (grant number 2304785).

**DECLARATION OF COMPETING INTERESTS**

The authors declare that they have no known competing financial interests or personal relationships that could have appeared to influence the work reported in this paper.

**DATA AVAILABILITY**

Data is available upon request.

# References


1. Gal-Katziri, M., Fikes, A. & Hajimiri, A. Flexible active antenna arrays. *npj Flexible Electronics* **6**, 85, doi:10.1038/s41528-022-00218-z (2022).
2. Hu, K., Zhou, Y., Sitaraman, S. K. & Tentzeris, M. M. Additively manufactured flexible on-package phased array antennas for 5G/mmWave wearable and conformal digital twin and massive MIMO applications. *Scientific Reports* **13**, 12515, doi:10.1038/s41598-023-39476-w (2023).
3. Niu, S. *et al.* A wireless body area sensor network based on stretchable passive tags. *Nature Electronics* **2**, 361-368, doi:10.1038/s41928-019-0286-2 (2019).
4. Zhu, J. *et al.* Stretchable wideband dipole antennas and rectennas for RF energy harvesting. *Materials Today Physics* **18**, 100377, doi:https://doi.org/10.1016/j.mtphys.2021.100377 (2021).
5. Chiang, Y. C. *et al.* Enhancing the high-frequency signal performance through surface morphological modification of Cu interconnects. *Measurement* **250**, 117071, doi:ARTN 11707110.1016/j.measurement.2025.117071 (2025).
6. Wheeler, H. A. Formulas for the Skin Effect. *Proceedings of the IRE* **30**, 412-424, doi:10.1109/JRPROC.1942.232015 (1942).
7. Formica, N. *et al.* Ultrastable and Atomically Smooth Ultrathin Silver Films Grown on a Copper Seed Layer. *ACS Appl. Mater. Interfaces* **5**, 3048-3053, doi:10.1021/am303147w (2013).
8. Shen, S. *et al.* Highly Conductive and Fatigue-Free Flexible Copper Film Electrode Fabricated by a Facile Dry Transfer Technique. *Adv Materials Inter* **5**, 1701038, doi:10.1002/admi.201701038 (2018).
9. Jeong, S. *et al.* Printable, stretchable metal-vapor-desorption layers for high-fidelity patterning in soft, freeform electronics. *Nat Commun* **15**, 7209, doi:10.1038/s41467-024-51585-2 (2024).
10. Islam, M. R. *et al.* Advances in Printed Electronic Textiles. *Advanced Science* **11**, 2304140, doi:10.1002/advs.202304140 (2024).
11. Kwon, Y.-T., Lee, Y.-I., Kim, S., Lee, K.-J. & Choa, Y.-H. Full densification of inkjet-printed copper conductive tracks on a flexible substrate utilizing a hydrogen plasma sintering. *Applied Surface Science* **396**, 1239-1244, doi:10.1016/j.apsusc.2016.11.122 (2017).
12. Shahariar, H. & Jur, J. S. Correlation of printing faults with the RF characteristics of coplanar waveguides (CPWs) printed on nonwoven textiles. *Sensors and Actuators A: Physical* **273**, 240-248, doi:10.1016/j.sna.2018.02.043 (2018).
13. Hong, H., Hu, J. & Yan, X. UV Curable Conductive Ink for the Fabrication of Textile-Based Conductive Circuits and Wearable UHF RFID Tags. *ACS Appl. Mater. Interfaces* **11**, 27318-27326, doi:10.1021/acsami.9b06432 (2019).
14. Beltran, V. V. *et al.* Enhancing the electric conductivity and surface smoothness of photosintered copper films on polyimide substrates. *Additive Manufacturing* **115**, 105072, doi:10.1016/j.addma.2025.105072 (2026).
15. Wang, C., Hossain Bhuiyan, M. E., Moreno, S. & Minary-Jolandan, M. Direct-Write Printing Copper–Nickel (Cu/Ni) Alloy with Controlled Composition from a Single Electrolyte Using Co-

Electrodeposition. *ACS Appl. Mater. Interfaces* **12**, 18683-18691, doi:10.1021/acsami.0c01100 (2020).

16. Bhuiyan, M. E. H. *et al.* A Hybrid Process for Printing Pure and High Conductivity Nanocrystalline Copper and Nickel on Flexible Polymeric Substrates. *Scientific Reports* **9**, 19032, doi:10.1038/s41598-019-55640-7 (2019).
17. Behroozfar, A. *et al.* Additive printing of pure nanocrystalline nickel thin films using room environment electroplating. *Nanotechnology* **31**, 055301, doi:10.1088/1361-6528/ab48bc (2020).
18. Jiao, Y. *et al.* Wash-stable electrospun piezopolymer textiles. *J of Applied Polymer Sci* **141**, e56205, doi:10.1002/app.56205 (2024).
19. Jiao, Y., Sepasi, Z., Khakzad, M. & Minary-Jolandan, M. Piezoelectric Nanofiber Mats With Enhanced Elastic Recovery for Smart Fabrics. *Advances in Polymer Technology* **2026**, 1005608, doi:https://doi.org/10.1155/adv/1005608 (2026).
20. Wang, Y. *et al.* Design and Manufacturing Principles of Smart Fibers. *Advanced Materials*, e73959, doi:10.1002/adma.73959 (2026).
21. Yang, E. *et al.* Nanofibrous Smart Fabrics from Twisted Yarns of Electrospun Piezopolymer. *ACS Appl. Mater. Interfaces* **9**, 24220-24229, doi:10.1021/acsami.7b06032 (2017).
22. Behroozfar, A. *et al.* Microscale 3D Printing of Nanotwinned Copper. *Advanced Materials* **30**, 1705107, doi:https://doi.org/10.1002/adma.201705107 (2018).
23. Daryadel, S., Behroozfar, A. & Minary-Jolandan, M. Toward Control of Microstructure in Microscale Additive Manufacturing of Copper Using Localized Electrodeposition. *Advanced Engineering Materials* **21**, 1800946, doi:https://doi.org/10.1002/adem.201800946 (2019).
24. Kongstein, O. E., Bertocci, U. & Stafford, G. R. In Situ Stress Measurements during Copper Electrodeposition on (111)-Textured Au. *Journal of The Electrochemical Society* **152**, C116, doi:10.1149/1.1854093 (2005).
25. Marro, J. B., Darroudi, T., Okoro, C. A., Obeng, Y. S. & Richardson, K. C. The influence of pulse plating frequency and duty cycle on the microstructure and stress state of electroplated copper films. *Thin Solid Films* **621**, 91-97, doi:https://doi.org/10.1016/j.tsf.2016.11.047 (2017).
26. Grujicic, D. & Pesic, B. Electrodeposition of copper: the nucleation mechanisms. *Electrochimica Acta* **47**, 2901-2912, doi:https://doi.org/10.1016/S0013-4686(02)00161-5 (2002).
27. Hu, C.-C. & Wu, C.-M. Effects of deposition modes on the microstructure of copper deposits from an acidic sulfate bath. *Surface and Coatings Technology* **176**, 75-83, doi:https://doi.org/10.1016/S0257-8972(03)00004-5 (2003).
28. Gleadall, A. FullControl GCode Designer: Open-source software for unconstrained design in additive manufacturing. *Additive Manufacturing* **46**, 102109, doi:https://doi.org/10.1016/j.addma.2021.102109 (2021).
29. Read, D. T., Cheng, Y. W. & Geiss, R. Morphology, microstructure, and mechanical properties of a copper electrodeposit. *Microelectronic Engineering* **75**, 63-70, doi:10.1016/j.mee.2003.09.012 (2004).

30. Min, H.-G., Kang, D.-J. & Park, J.-H. Comparison of Tensile and Fatigue Properties of Copper Thin Film Depending on Process Method. *Applied Sciences* **10**, 388, doi:10.3390/app10010388 (2020).
31. Lee, Y.-S., Ha, S., Park, J.-H. & Lee, S.-B. Structure-dependent mechanical behavior of copper thin films. *Materials Characterization* **128**, 68-74, doi:10.1016/j.matchar.2017.03.036 (2017).
32. Dong, G. *et al.* Thickness-dependent microstructure evolution and mechanical properties of electrodeposited copper foils. *Journal of Materials Research and Technology* **42**, 3411-3422, doi:10.1016/j.jmrt.2026.04.039 (2026).
33. Chan, H.-J., Huang, B.-C., Wang, L.-W., Liao, K.-H. & Lo, C.-Y. Porosity reduction in inkjet-printed copper film by progressive sintering on nanoparticles. *Thin Solid Films* **627**, 33-38, doi:10.1016/j.tsf.2017.02.062 (2017).
34. Lee, W. H., Chen, Y.-X. & Lin, H. H. A novel electrochemical deposition of copper conductor on flexible printed circuit boards. *Electrochemistry Communications* **183**, 108090, doi:10.1016/j.elecom.2025.108090 (2026).
35. Hammerstad, E. & Jensen, O. in *1980 IEEE MTT-S International Microwave symposium Digest.* 154.
36. Jang, Y.-R., Jeong, R., Kim, H.-S. & Park, S. S. Fabrication of solderable intense pulsed light sintered hybrid copper for flexible conductive electrodes. *Scientific Reports* **11**, 14551, doi:10.1038/s41598-021-94024-8 (2021).
37. Kang, J. S. *et al.* Inkjet printed electronics using copper nanoparticle ink. *J Mater Sci: Mater Electron* **21**, 1213-1220, doi:10.1007/s10854-009-0049-3 (2010).
38. Kim, Y. *et al.* Use of copper ink for fabricating conductive electrodes and RFID antenna tags by screen printing. *Current Applied Physics* **12**, 473-478, doi:10.1016/j.cap.2011.08.003 (2012).
39. Olsen, E. & Overmeyer, L. Laser sintering of copper conductive traces on primer pre-treated additive manufactured 3D surfaces. *Flex. Print. Electron.* **6**, 015006, doi:10.1088/2058-8585/abdbfd (2021).
40. Pervan, D. *et al.* Additive Manufacturing of Electrically Conductive Multi-Layered Nanocopper in an Air Environment. *Nanomaterials* **14**, 753, doi:10.3390/nano14090753 (2024).

# Figures

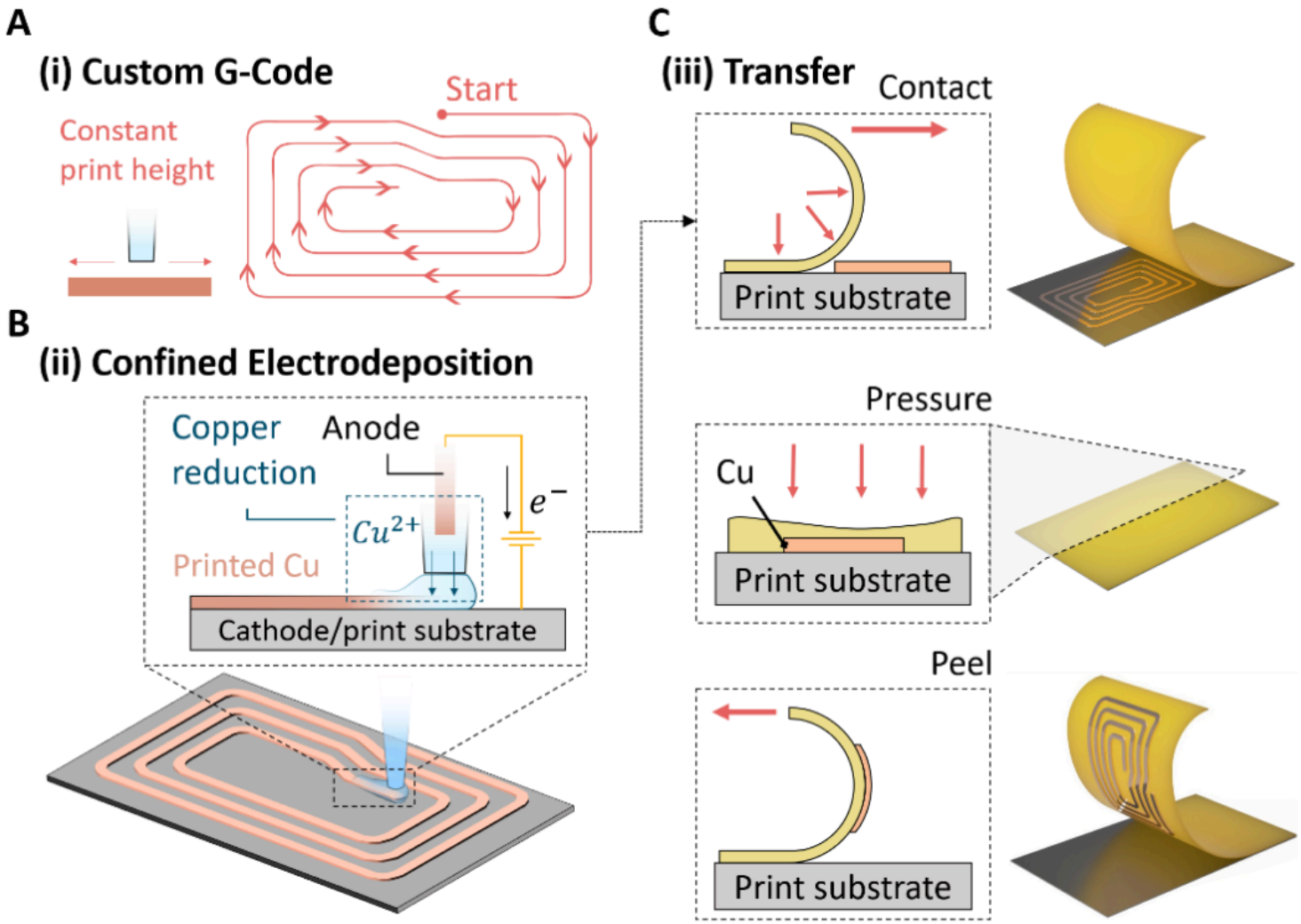



**Figure 1**

Meniscus-confined electrodeposition and transfer printing of copper. The process comprises three sequential steps, labeled (i)–(iii). (A) Step (i): a user-defined G-code toolpath, executed at constant print height, defines the planar copper geometry. (B) Step (ii): confined electrodeposition. Electrolyte is confined to a meniscus beneath an anode-bearing nozzle, restricting copper deposition to the wetted footprint on the stainless-steel cathode/print substrate. (C) Step (iii): transfer. The transfer substrate is brought into contact with the printed copper (Contact), pressure is applied uniformly across the film (Pressure), and peeling exploits the differential adhesion between the copper-tape and copper-steel interfaces to lift the film cleanly onto the receiver substrate (Peel).

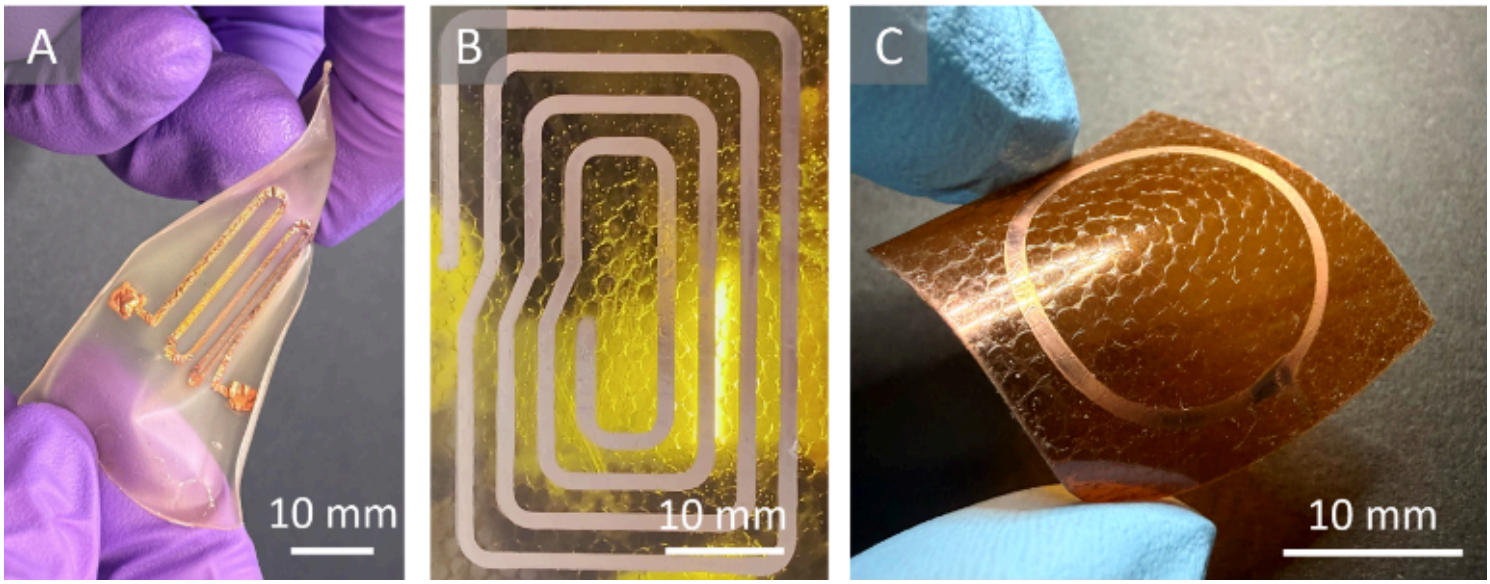



**Figure 2**

Copper patterns transferred onto various substrates. (A) Serpentine pattern with bonding pads transferred onto a cast PVDF-TrFE film. (B) Spiral of filleted concentric rectangular tracks transferred onto a Kapton tape substrate. (C) Circular loop transferred onto a Kapton tape substrate.

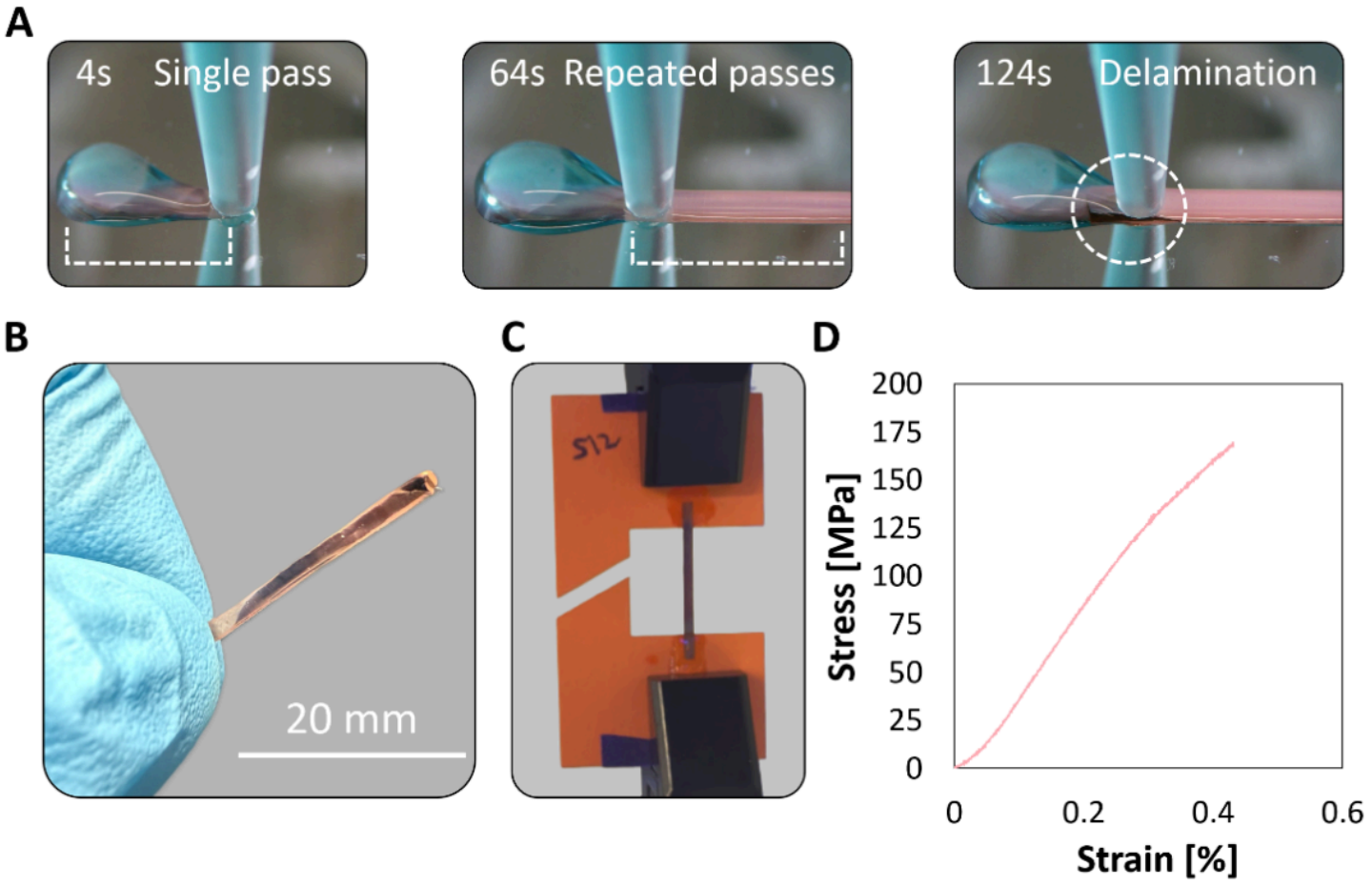
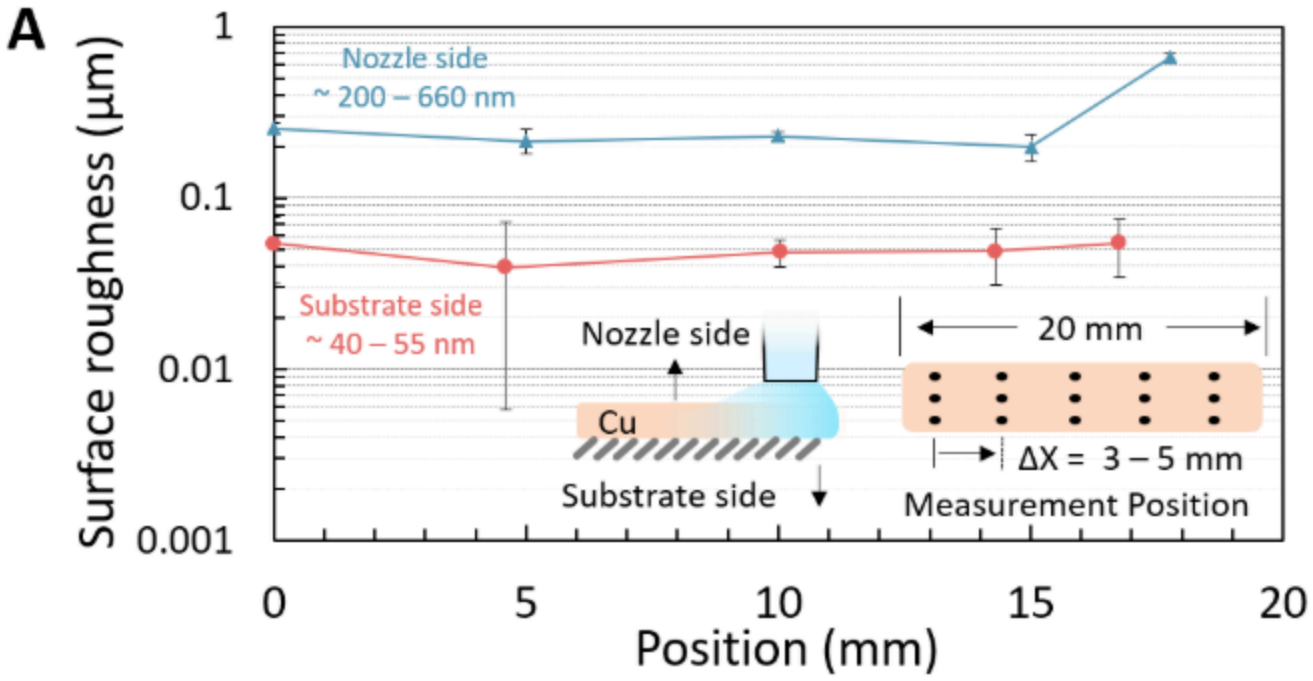
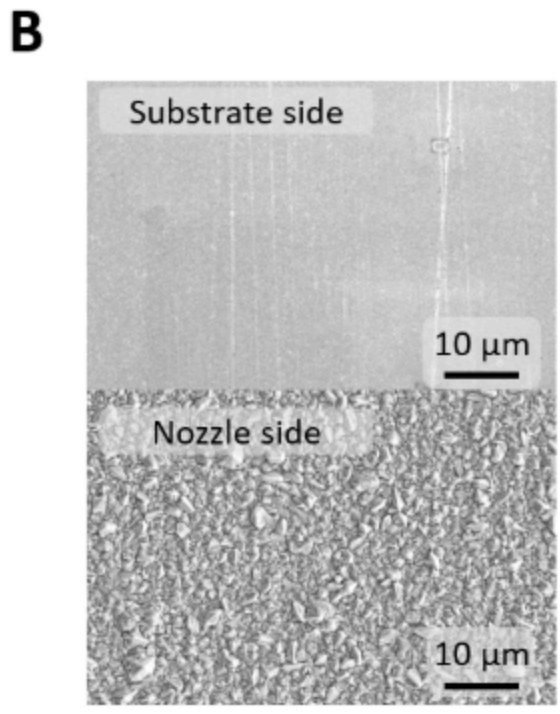



**Figure 3**

Mechanical integrity and handleability of delaminated copper films. (A) Time-lapse optical images of meniscus-confined electrodeposition of a copper line on stainless steel at 4 s (single pass), 64 s (repeated passes), and 124 s (delamination onset). White dashed boxes highlight the growing copper deposit beneath the nozzle in the first two frames; the white dashed circle at 124 s marks spontaneous delamination at the terminal end of the trace. (B) Delaminated copper film handled as a free-standing foil, demonstrating sufficient mechanical integrity for transfer. Scale bar, 20 mm. (C) Optical image of a copper film mounted between tensile test grips on a Kapton tape carrier. (D) Representative stress–strain curve of a free-standing copper film.



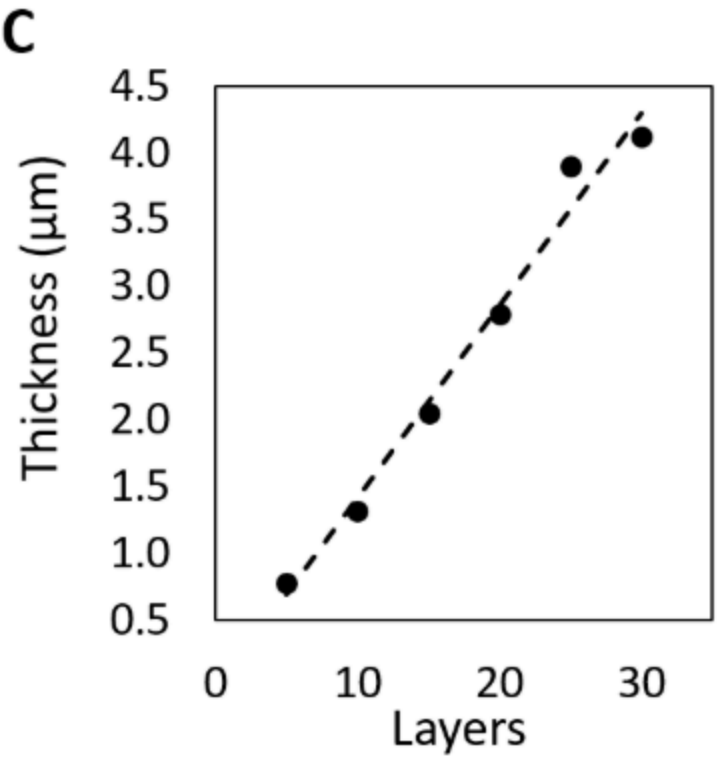



**Figure 4**

Surface morphology and thickness control of delaminated confined-electrodeposited copper. (A) Surface roughness along the 20 mm trace measured by laser confocal microscopy at a 3×5 grid (three positions across the width at edges and center, five along the length at ~3–5 mm spacing; inset). The substrate side is smooth and position-independent (Sq 40–55 nm); the nozzle side is rougher and more variable (Sq 200–660 nm), rising toward the terminal end. The inset also shows the deposition schematic indicating the two measured faces. (B) SEM of the two faces: substrate side (top) smooth and featureless, reproducing the polished steel finish; nozzle side (bottom) granular and nodular. Scale bars, 10 μm. (C) Film thickness versus pass count; growth is linear at ~0.13 μm per layer from ~0.75 μm at 5 layers to ~4.1 μm at 30 layers. Dashed line, linear fit.

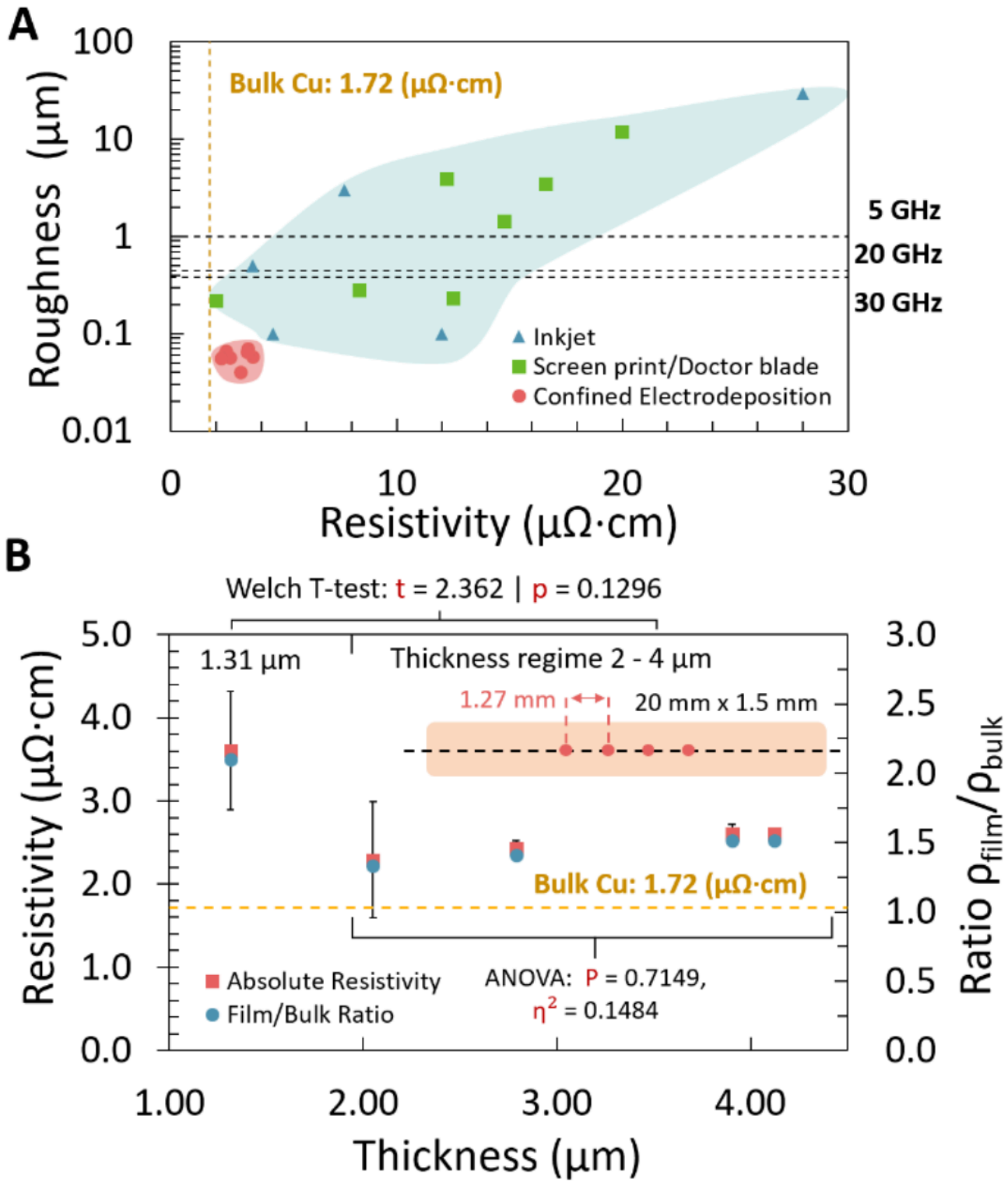



**Figure 5**

Electrical quality of delaminated confined-electrodeposited copper. (A) Roughness versus resistivity for confined electrodeposition (this work), inkjet, and screen-print/doctor-blade copper. Confined-electrodeposited copper occupies the lower left corner, combining lower roughness and lower resistivity than all printed routes. Vertical dashed line, bulk copper resistivity (1.72 µΩ·cm); horizontal dashed lines, copper skin depth at 5, 20, and 30 GHz. (B) Four-point-probe resistivity (red squares, left axis) and film-to-

bulk resistivity ratio (blue circles, right axis) versus film thickness. Resistivity is statistically flat across 2–4 μm at ~1.3–1.5× bulk (one-way ANOVA, P = 0.71, $\eta^2$ = 0.15); the thinnest film (1.31 μm) measures higher but is not significantly different from thicker films (Welch's t-test, $t$ = 2.36, $P$ = 0.13). Dashed line, bulk copper resistivity; inset, four-point probe geometry (1.27 mm contact spacing, 20 mm × 1.5 mm deposit) [11,13,14,33,34,36-40].

## Supplementary Files

This is a list of supplementary files associated with this preprint. Click to download.

- SI.docx
- VideoS2.mp4
- VideoS1.mp4